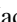







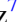

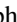












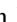






# JWST’s TEMPLATES for Star Formation: The First Resolved Gas-phase Metallicity Maps of Dust-obscured Star-forming Galaxies at $z \sim 4$

Jack E. Birkin<sup>1</sup> , Taylor A. Hutchison<sup>2,25</sup> , Brian Welch<sup>2,3,4</sup> , Justin S. Spilker<sup>1</sup> , Manuel Aravena<sup>5</sup> ,  
Matthew B. Bayliss<sup>6</sup> , Jared Cathey<sup>7</sup> , Scott C. Chapman<sup>8,9,10</sup> , Anthony H. Gonzalez<sup>7</sup> , Gayathri Gururajan<sup>11,12</sup> ,  
Christopher C. Hayward<sup>13</sup> , Gourav Khullar<sup>14</sup> , Keunho J. Kim<sup>6</sup> , Guillaume Mahler<sup>15,16</sup> , Matthew A. Malkan<sup>17</sup> ,  
Desika Narayanan<sup>7,18</sup> , Grace M. Olivier<sup>1</sup> , Kedar A. Phadke<sup>19,20</sup> , Cassie Reuter<sup>19</sup> , Jane R. Rigby<sup>2</sup> , J. D. T. Smith<sup>21</sup> ,  
Manuel Solimano<sup>22</sup> , Nikolaus Sulzenauer<sup>23</sup> , Joaquin D. Vieira<sup>19,20,24</sup> , David Vizgan<sup>19</sup> , and Axel Weiss<sup>23</sup> 

<sup>1</sup> Department of Physics and Astronomy and George P. and Cynthia Woods Mitchell Institute for Fundamental Physics and Astronomy, Texas A&M University, 4242 TAMU, College Station, TX 77843-4242, USA;

<sup>2</sup> Observational Cosmology Lab, Code 665, NASA Goddard Space Flight Center, 8800 Greenbelt Road, Greenbelt, MD 20771, USA

<sup>3</sup> Department of Astronomy, University of Maryland, College Park, MD 20742, USA

<sup>4</sup> Center for Research and Exploration in Space Science and Technology, NASA/GSFC, Greenbelt, MD 20771, USA

<sup>5</sup> Instituto de Estudios Astrofísicos, Facultad de Ingeniería y Ciencias, Universidad Diego Portales, Av Ejército 441, Santiago, Chile

<sup>6</sup> Department of Physics, University of Cincinnati, Cincinnati, OH 45221, USA

<sup>7</sup> Department of Astronomy, University of Florida, 211 Bryant Space Sciences Center, Gainesville, FL 32611 USA

<sup>8</sup> Department of Physics and Astronomy, University of British Columbia, 6225 Agricultural Road, Vancouver V6T 1Z1, Canada

<sup>9</sup> National Research Council, Herzberg Astronomy and Astrophysics, 5071 West Saanich Road, Victoria V9E 2E7, Canada

<sup>10</sup> Department of Physics and Atmospheric Science, Dalhousie University, 6310 Coburg Road, B3H 4R2 Halifax, Canada

<sup>11</sup> Department of Physics and Astronomy “Augusto Righi” (DIFA), University of Bologna, Via Gobetti 93/2, I-40129 Bologna, Italy

<sup>12</sup> INAF—Osservatorio di Astrofisica e Scienza dello Spazio, Via Gobetti 93/3, I-40129 Bologna, Italy

<sup>13</sup> Center for Computational Astrophysics, 162 Fifth Avenue, New York, NY 10010, USA

<sup>14</sup> Department of Physics and Astronomy and PITT PACC, University of Pittsburgh, Pittsburgh, PA 15260, USA

<sup>15</sup> Centre for Extragalactic Astronomy, Durham University, South Road, Durham DH1 3LE, UK

<sup>16</sup> Institute for Computational Cosmology, Durham University, South Road, Durham DH1 3LE, UK

<sup>17</sup> Department of Physics and Astronomy, University of California, Los Angeles, 430 Portola Plaza, Los Angeles, CA 90095, USA

<sup>18</sup> Cosmic Dawn Center at the Niels Bohr Institute, University of Copenhagen and DTU-Space, Technical University of Denmark, Denmark

<sup>19</sup> Department of Astronomy, University of Illinois, 1002 West Green Street, Urbana, IL 61801, USA

<sup>20</sup> Center for Astrophysical Surveys, National Center for Supercomputing Applications, 1205 West Clark Street, Urbana, IL 61801, USA

<sup>21</sup> University of Toledo Department of Physics and Astronomy, Ritter Astrophysical Research Center, Toledo, OH 43606, USA

<sup>22</sup> Instituto de Estudios Astrofísicos, Facultad de Ingeniería y Ciencias, Universidad Diego Portales, Avenida Ejército Libertador 441, Santiago 8370191, Chile

<sup>23</sup> Max-Planck-Institut für Radioastronomie, Auf dem Hügel 69, D-53121 Bonn, Germany

<sup>24</sup> Department of Physics, University of Illinois, 1110 West Green Street, Urbana, IL 61801, USA; [jbirkin@tamu.edu](mailto:jbirkin@tamu.edu)

Received 2023 June 5; revised 2023 August 21; accepted 2023 August 24; published 2023 December 5

## Abstract

We present the first spatially resolved maps of gas-phase metallicity for two dust-obscured star-forming galaxies at  $z \sim 4$ , from the JWST TEMPLATES Early Release Science program, derived from NIRSpect integral field unit spectroscopy of the  $H\alpha$  and [N II] emission lines. Empirical optical line calibrations are used to determine that the sources are globally enriched to near-solar levels. While one source shows elevated [N II]/ $H\alpha$  ratios and broad  $H\alpha$  emission consistent with the presence of an active galactic nucleus in a  $\gtrsim 1$  kpc region, we argue that both systems have already undergone significant metal enrichment as a result of their extremely high star formation rates. Utilizing Atacama Large Millimeter/submillimeter Array rest-frame  $380 \mu\text{m}$  continuum and [CI]( $^3P_2$ – $^3P_1$ ) line maps we compare the spatial variation of the metallicity and gas-to-dust ratio in the two galaxies, finding the two properties to be anticorrelated on highly resolved spatial scales, consistent with various literature studies of  $z \sim 0$  galaxies. The data are indicative of the enormous potential of JWST to probe the enrichment of the interstellar medium on  $\sim$ kpc scales in extremely dust-obscured systems at  $z \sim 4$  and beyond.

*Unified Astronomy Thesaurus concepts:* Galaxy evolution (594); High-redshift galaxies (734); Galaxy formation (595); Starburst galaxies (1570); Strong gravitational lensing (1643)

## 1. Introduction

At so-called “cosmic noon” ( $z \sim 2$ ) and beyond, a significant fraction of the Universe’s star formation occurs in dust-obscured star-forming galaxies (DSFGs; Casey et al. 2014; Swinbank et al. 2014; Dudzevičiūtė et al. 2020; Zavala et al.

2021). In such systems, the majority of the rest-frame optical and ultraviolet (UV) light associated with young stars is absorbed by dust and reprocessed into the far-infrared.

Multiwavelength analyses and molecular gas observations have revealed that DSFGs are massive, gas rich and highly star forming, with IR luminosities  $L_{\text{IR}} > 10^{12} L_{\odot}$ , implied star formation rates (SFRs) of  $100$ – $1000 M_{\odot} \text{ yr}^{-1}$  (see, e.g., Swinbank et al. 2014; Spilker et al. 2015; Aravena et al. 2016; Strandet et al. 2017; Dudzevičiūtė et al. 2020; Reuter et al. 2020; Birkin et al. 2021) and dense interstellar media (ISMs; e.g., Spilker et al. 2014; Birkin et al. 2021; Rybak et al. 2022; Reuter et al. 2023). The observed properties of DSFGs (such as

<sup>25</sup> NASA Postdoctoral Fellow.

their high IR luminosities) and the fact that sources have been detected up to  $z \sim 7$  has made them challenging to reproduce in current models of galaxy formation and evolution (Davé et al. 2010; Lacey et al. 2016; McAlpine et al. 2019; Hayward et al. 2021; Bassini et al. 2023). Therefore, observations of DSFGs can provide strong constraints on such theories.

The ISM plays a critical role in the ongoing processes within DSFGs, such as star formation, supernovae, and winds, which add, remove, and redistribute metals. Therefore, measuring the gas-phase metallicity and its variation across the galaxy is a powerful indicator of its past evolution (e.g., Maiolino & Mannucci 2019), for example through scaling relations such as the mass-metallicity relation (MZR; e.g., Tremonti et al. 2004) and fundamental metallicity relation (FMR; e.g., Mannucci et al. 2010; Curti et al. 2020). A simple and effective method for estimating metallicity is to measure the relative strengths of the [N II] and H $\alpha$  emission lines (e.g., Pettini & Pagel 2004; Marino et al. 2013; Dopita et al. 2016; Maiolino & Mannucci 2019), which suffer similar levels of dust extinction due to their close proximity in wavelength. This method has limitations, such as being highly sensitive to the ionization parameter and N/O abundance (Pérez-Montero & Contini 2009; Dopita et al. 2016; Pilyugin & Grebel 2016; Peng et al. 2021), but the brightness of these lines and their accessibility at high redshifts have made them popular observables for metallicity (e.g., Steidel et al. 2014; Sanders et al. 2015; Gillman et al. 2022).

The launch of JWST and its successful commissioning (Rigby et al. 2023a, 2023b; Gardner et al. 2023; McElwain et al. 2023; Menzel et al. 2023) have transformed our ability to study galaxy formation and evolution, and we are now entering a new era for extragalactic astronomy. JWST’s Near-Infrared Spectrograph (NIRSpec; Böker et al. 2023) can study high-redshift galaxies at sub-kpc spatial resolution, offering a vast improvement over previous ground-based (and therefore seeing-limited) studies. Additionally, at high redshifts the spectral coverage of NIRSpec encompasses the key emission lines that trace gas-phase metallicity such as H $\alpha$ , [N II]  $\lambda$ 6584, [O III]  $\lambda$ 5007, 4958, H $\beta$ , [S II]  $\lambda$ 6717, 6731, [O II]  $\lambda$ 3727, 3729 and [Ne III]  $\lambda$ 3870 (e.g., Wuyts et al. 2014; Maiolino & Mannucci 2019; Sanders et al. 2020).

At high redshifts, strong gravitational lensing due to massive foreground structures allows us to observe galaxies at higher spatial resolution than would otherwise be possible. This technique is commonly used to study the DSFG population, with modest samples of lensed sources characterized by Herschel, Planck, the Atacama Cosmology Telescope (ACT), the South Pole Telescope (SPT; e.g. Negrello et al. 2010; Vieira et al. 2013; Marsden et al. 2014; Busmann et al. 2015; Harrington et al. 2016; Spilker et al. 2016; Everett et al. 2020; Kamieneski et al. 2023), and through the Atacama Large Millimeter/submillimeter Array (ALMA) Cluster Lensing Survey (ALCS; e.g., Sun et al. 2022). Many sources have been detected up to  $z \sim 7$  (e.g., Marrone et al. 2018; Reuter et al. 2020; Endsley et al. 2023).

In this work, we present Director’s Discretionary Early Release Science (DD-ERS) NIRSpec IFU observations of two SPT-selected gravitationally lensed DSFGs: SPT0418-17 at  $z = 4.2246$  and SPT2147-50 at  $z = 3.7604$  (Reuter et al. 2020), with which we demonstrate the significant advancements that JWST is already providing in our study of this population. The outline of this paper is as follows: in Section 2 we describe the observations carried out, our data reduction methods, and our analysis of the reduced data. In Section 3 we present the results

**Table 1**  
Summary of the Key Properties for Both DSFGs Studied in This Work

|   | SPT0418-47                     | SPT2147-50                     |
|---|--------------------------------|--------------------------------|
| R.A.  | 04:18:39.67                    | 21:47:19.05                    |
| Decl.                                       | −47:51:52.5                    | −50:35:53.5                    |
| $\mu$                                       | $29.5 \pm 1.2$                 | $6.6 \pm 0.4$                  |
| $\mu$ SFR/ $M_{\odot}$ yr $^{-1}$           | $3770 \pm 545$                 | $4630 \pm 230$                 |
| $\mu M_{*}/M_{\odot}$                       | $(4.5 \pm 0.9) \times 10^{11}$ | $(4.2 \pm 1.0) \times 10^{11}$ |
| $A_V$                                       | $3.8 \pm 0.1$                  | $2.5 \pm 0.1$                  |
| $z$   | 4.2246(4)                      | 3.7604(2)                      |
| Whole Source                                |                                |                                |
| [N II]/H $\alpha$                           | $0.43 \pm 0.03$                | $0.62 \pm 0.04$                |
| [S II]/H $\alpha$                           | $0.23 \pm 0.01$                | $0.24 \pm 0.01$                |
| $12 + \log(\text{O}/\text{H})_{\text{M13}}$ | $8.57 \pm 0.16$                | $8.65 \pm 0.16$                |
| $Z_{\text{M13}} / Z_{\odot}$                | $0.8 \pm 0.3$                  | $0.9 \pm 0.3$                  |
| Masking [N II]/H $\alpha$ > 0.5             |                                |                                |
| [N II]/H $\alpha$                           | $0.34 \pm 0.02$                | $0.53 \pm 0.02$                |
| [S II]/H $\alpha$                           | $0.21 \pm 0.01$                | $0.23 \pm 0.01$                |
| $12 + \log(\text{O}/\text{H})_{\text{M13}}$ | $8.53 \pm 0.16$                | $8.55 \pm 0.16$                |
| $Z_{\text{M13}}/Z_{\odot}$                  | $0.7 \pm 0.3$                  | $0.7 \pm 0.3$                  |

**Notes.** Magnification values are taken from Cathey et al. (2023) for SPT0418-47 and Spilker et al. (2016) for SPT2147-50. The SFRs, stellar masses, and dust attenuations are derived from SED fitting with CIGALE (Cathey et al. 2023; K. A. Phadke et al. 2023, in preparation). Redshifts are taken from Reuter et al. (2020). For the  $12 + \log(\text{O}/\text{H})$  calibrations, we quote the scatter of the M13 calibration (0.16 dex) as the uncertainty, which is much more significant than the uncertainties on our line ratio measurements.

and discuss their implications. In Section 4 we summarize our findings. Throughout this paper we adopt the cosmology measured by Planck Collaboration et al. (2020), i.e., flat with  $\Omega_m = 0.310$  and  $H_0 = 67.7 \text{ km s}^{-1} \text{ Mpc}^{-1}$ , and a solar metallicity of  $12 + \log(\text{O}/\text{H}) = 8.69$  (Asplund et al. 2021).

## 2. Observations, Data Reduction, and Analysis

### 2.1. JWST

The JWST/NIRSpec observations are drawn from the DD-ERS program Targeting Extremely Magnified Panchromatic Lensed Arcs and Their Extended Star formation (TEMPLATES; Program 1355; PI: J. Rigby; Co-PI: J. Vieira). From TEMPLATES we utilize NIRSpec IFU G395M/F290LP observations of two SPT-selected DSFGs: SPT0418-47 and SPT2147-50. From spectral energy distribution (SED) fitting it is known that both galaxies are highly massive and highly star forming (Cathey et al. 2023; see Table 1).

The JWST data used in this manuscript can be found in MAST at [10.17909/fdje-fq59](https://mast.stsci.edu/portal/#docinfo/doisdetail?doi=10.17909/fdje-fq59). We reduce the data with the standard JWST pipeline (version 1.10.2; Bushouse et al. 2023) using calibration reference data system (CRDS) context `jwst_1089.pmap`, with some modifications. Full details on the TEMPLATES data reduction will be provided in J. R. Rigby et al. (2023, in preparation), but here we describe how our process differs from the standard pipeline. We modify the outlier detection stage of the pipeline as we found that in some cases the default stage can remove real signal. In our alternate sigma clipping method we first mask the galaxy and clip the background, and then perform the same process on layers of the galaxy of increasing signal-to-noise ratio (S/N). This layering was chosen to ensure that spaxels with weaker emission did not

affect the clipping of spaxels with strong emission. We also applied a small offset ( $\sim 0''.5$  for both sources) to match the data to ALMA rest-frame  $380\ \mu\text{m}$  continuum data (see Section 2.2). These astrometric shifts were determined by comparing the coordinates of the central continuum source with Hubble Space Telescope/WFC3 F140W imaging (Ma et al. 2015).

As part of our analysis we also generate NIRSpec cubes with  $0''.5$  resolution (as opposed to the original  $\sim 0''.1$  resolution). This is done to ensure consistency with existing ALMA data (see Section 2.2), which we use to derive maps of the dust and gas emission. To generate the  $0''.5$  resolution NIRSpec cubes we convolve the original ( $0''.1$  pixel scale) cubes with a circular Gaussian point-spread function (PSF) of  $\text{FWHM} = 0''.49$ . The target spatial resolution ( $0''.5$ , and Gaussian by construction) is sufficiently poorer than the intrinsic JWST PSF ( $0''.1$ ) that the wings and spikes in the JWST PSF can be safely ignored.

## 2.2. ALMA

To supplement the data from JWST/NIRSpec, we utilize ALMA data covering the rest-frame  $380\ \mu\text{m}$  continuum emission and the  $[\text{Cl}](^3\text{P}_2-^3\text{P}_1)$  line emission, which will be used in Section 3.3 as proxies for dust mass and gas mass, respectively. For SPT0418-47 we utilize Band 4 data from program 2021.1.00252.S (PI: J. Vieira), which we image using natural weighting and taper to a spatial resolution of  $0''.5$ , creating continuum images and  $\text{CO}(7-6)/[\text{Cl}](2-1)$  cubes. For SPT2147-50 we utilize Band 5 data from program 2018.1.01060.S (PI: J. Vieira) which is processed in the same way, except the imaging was performed using Briggs weighting with a robust parameter of 0.45. This enabled us to achieve the same resolution as the SPT0418-47 data.

## 2.3. Resolved Fitting

To achieve our goal of determining how the metallicity varies across our two targets, we model the  $\text{H}\alpha$  and  $[\text{N II}]$  complex as a triple-Gaussian profile, on a pixel-by-pixel basis, tying the wavelengths of the emission and coupling their line widths, with the  $\text{H}\alpha/[\text{N II}]$  flux ratio left as a free parameter. The flux ratio of  $[\text{N II}]\ \lambda 6584/[\text{N II}]\ \lambda 6548$  is fixed at 2.8 (Osterbrock & Ferland 2006), and we also include a constant continuum component. We attempt to model the emission lines in each pixel, and if we measure an S/N of at least eight across the  $\text{H}\alpha+[\text{N II}]$  complex the pixel is included in the flux maps. Otherwise, the pixel is ignored, and not used in our subsequent analysis. The threshold of  $\text{S/N} = 8$  was chosen through trial and error, to minimize pixels where the apparent  $\text{H}\alpha$  emission is largely due to noise while ensuring that the derived flux maps contain enough pixels to study the resolved properties. To boost the S/N we bin each spaxel with its eight neighboring spaxels. Finally, we visually inspect the resultant  $\text{H}\alpha$  flux maps along with the fits to each spaxel, and mask by hand any spaxels where the emission does not appear to be coming from the target galaxy. This includes masking emission from a newly detected companion galaxy (Peng et al. 2022; Cathey et al. 2023; see Section 3.1), which we elect not to study in detail in this work.

## 3. Results and Discussion

Figure 1 shows the 1D spectra extracted from the two DSFGs in pixels where  $\text{H}\alpha$  and  $[\text{N II}]$  are detected, and Figure 2 shows the same spectra, but this time zoomed into the

$\text{H}\alpha$ ,  $[\text{N II}]$ , and  $[\text{S II}]$  lines. We show both the integrated spectra, and a sample spaxel (binned with neighboring spaxels) for each galaxy. The  $[\text{S II}]$  doublet is shown with a double-Gaussian fit in the integrated spectra as it is clearly detected, but the S/N is insufficient to detect it in individual pixels. Therefore we do not model  $[\text{S II}]$  in our resolved fitting. The triple-Gaussian fit models the  $\text{H}\alpha$  and  $[\text{N II}]$  lines well in both cases. The resultant maps of  $\text{H}\alpha$  and  $[\text{N II}]$  emission are shown in Figures 3 and 4 for SPT0418-47 and SPT2147-50, respectively. We detect continuum emission across the observed wavelength range in both sources, a combination of stellar continuum from the background DSFGs and light from the bright foreground lenses blurred into the background emission by the JWST PSF. We model the continuum using a running median with a window size large enough so as to avoid removing any flux from the emission lines ( $\sim 10,000\ \text{km s}^{-1}$ ). Both DSFGs display strong  $\text{H}\alpha$  and  $[\text{N II}]\ \lambda 6584$  emission, along with the  $[\text{S II}]\ \lambda\lambda 6717, 6731$  and  $[\text{S III}]\ \lambda\lambda 9071, 9533$  doublets. Additionally, in the lower-redshift SPT2147-50 we detect  $\text{He I}$  and  $\text{Pa}\gamma$  emission, with tentative evidence for  $\text{Pa}\delta$ .

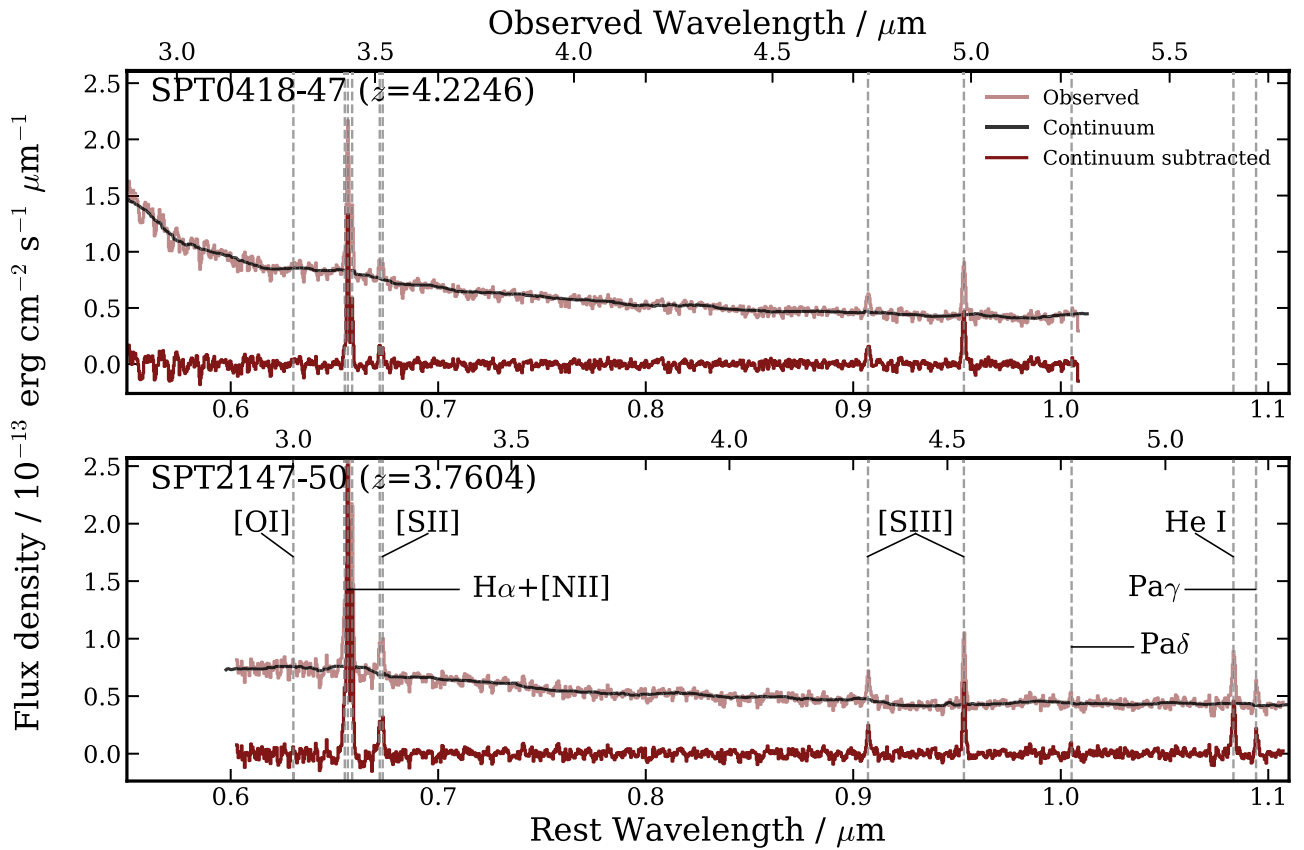
## 3.1. Line Ratios and Metallicities

To derive metallicities for the two DSFGs we first convert the  $[\text{N II}]\ \lambda 6584/\text{H}\alpha$  ratio from the line fits to an oxygen abundance  $12 + \log(\text{O}/\text{H})$  using the calibration for  $\text{N2} \equiv \log_{10}([\text{N II}]/\text{H}\alpha)$  as derived by Marino et al. (2013; hereafter M13):

$$12 + \log(\text{O}/\text{H})_{\text{M13}} = 8.743 + 0.462 \text{N2}, \quad (1)$$

which is derived from a fit to 452 H II regions with  $T_e$ -based metallicity measurements. The regions considered are valid up to  $\text{N2} = -0.2$  or  $[\text{N II}]/\text{H}\alpha \sim 0.63$ . A number of other calibrations were considered, including those proposed by Pettini & Pagel (2004; hereafter PP04), Curti et al. (2020; hereafter C20) and Dopita et al. (2016; hereafter D16), the latter of which also uses the  $[\text{S II}]$  doublet. We selected the M13 calibration as it is considered more reliable at high redshifts and in better agreement with other calibrations than PP04 (e.g., Poetrodjojo et al. 2021), and is simpler to extrapolate to higher metallicities than C20, who used a fourth-order polynomial fit which is not well constrained in the high-metallicity regime. As an alternative measurement we briefly discuss results using the D16 calibration, but as the S/Ns of our  $[\text{S II}]$  detections are low we are unable to use this line on a spatially resolved basis. Therefore for consistency we primarily use the M13 calibration. We note here that while we later study the global MZR and FMR, our main concern in this work is the spatial variation of the metallicity with other properties rather than their absolute values.

As the  $[\text{N II}]/\text{H}\alpha$  ratio is very high ( $>0.8$ ) in several regions of both sources, we cannot rule out active galactic nuclei (AGN) as being responsible for this emission. In SPT2147-50 this is supported by very broad FWHMs ( $\sim 800\ \text{km s}^{-1}$ ) which correspond with regions of high  $[\text{N II}]/\text{H}\alpha$ . This could be evidence for AGN-driven winds in this system. No previous work on these two sources has suggested that either are AGN hosts (e.g., Bothwell et al. 2017; De Breuck 2019). The same is true for other DSFGs from the same parent sample (Ma et al. 2016; Apostolovski et al. 2019). Therefore, this is a surprising



**Figure 1.** One-dimensional JWST/NIRSpec rest-frame spectra of SPT0418-47 and SPT2147-50, displaying strong detections of the  $H\alpha$  and  $[N II]$  emission lines, in addition to the  $[S III]$  doublet. Both spectra are extracted only from spaxels where  $H\alpha + [N II]$  is detected with  $S/N > 8$ . SPT2147-50 displays detections of the He I line and  $Pa\gamma$  lines, and marginal evidence for  $Pa\delta$  emission. Neither of the sources are detected in  $[O I]$ .

result, particularly for SPT2147-50 which shows the highest  $[N II]/H\alpha$  ratios.

Galaxies are commonly classified as AGN dominated or otherwise using the Baldwin, Phillips, and Terlevich (BPT; Baldwin et al. 1981) diagram (e.g., Kewley et al. 2006). However, the other BPT diagnostics  $[O III]$  and  $H\beta$  (neither of which fall within the coverage of our data) are needed to confirm this. Even with these additional diagnostics, the boundary between star-forming galaxies and AGN in the BPT diagram is uncertain at  $z \sim 2$ , let alone at  $z \sim 4$  where the two DSFGs reside (Kewley et al. 2013). We therefore also derive metallicities masking out individual pixels with  $[N II]/H\alpha > 0.5$ , which we choose to provide a conservative lower limit on the integrated metallicity.

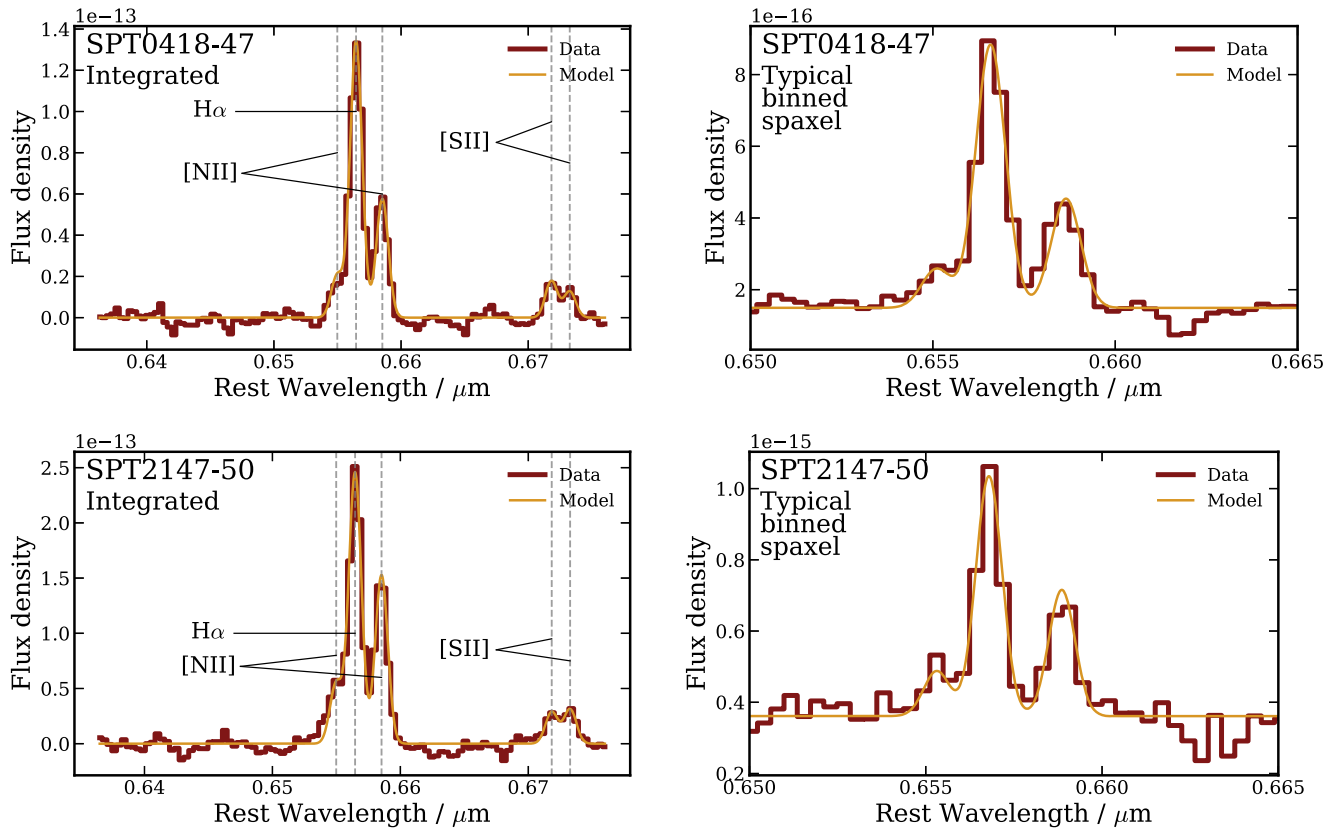
In the former case, i.e., using all pixels with  $H\alpha$  detections, and based on the M13 calibration, SPT0418-47 has  $12 + \log(O/H) = 8.57 \pm 0.16$  and  $Z = 0.8 \pm 0.3 Z_{\odot}$ , respectively. SPT2147-50 has  $12 + \log(O/H) = 8.65 \pm 0.16$  and  $Z = 0.9 \pm 0.3 Z_{\odot}$ , respectively. Adopting a conservative cutoff of  $[N II]/H\alpha > 0.5$  (which masks  $\sim 43\%$  and  $\sim 70\%$  of the pixels in SPT0418-47 and SPT2147-50, respectively) these values change to  $Z = 0.7 \pm 0.3 Z_{\odot}$  for SPT0418-47 and  $Z = 0.7 \pm 0.3 Z_{\odot}$  for SPT2147-50. Interestingly, applying this correction does not significantly change the global metallicity values; both are still a significant fraction of the solar value, and consistent with solar abundances in all cases.

The detections of  $[S II] \lambda\lambda 6717, 6731$  are significant enough in the integrated spectra of both galaxies (see Figure 2) to provide an independent estimate of the metallicity. Additionally,  $[S II]$  is sufficiently close in wavelength to  $H\alpha$  and  $[N II]$

that any extinction corrections would be negligible. We therefore also apply the D16 calibration for  $H\alpha$ ,  $[N II]$ , and  $[S II]$  to estimate  $12 + \log(O/H)$ . Interestingly, this calibration gives significantly higher values of metallicity:  $Z = 1.8 \pm 0.7 Z_{\odot}$  for SPT0418-47 and  $Z = 2.7 \pm 1.0 Z_{\odot}$  for SPT2147-50 (decreasing to  $1.5 \pm 0.6 Z_{\odot}$  and  $1.7 \pm 0.7 Z_{\odot}$ , respectively, when applying our AGN masking). The D16 calibration has been claimed to have a reduced dependence on the ionization parameter when compared to N2, and therefore this is further evidence that the two DSFGs are highly enriched with metals, possibly even to solar or super-solar levels.

We note that the two  $[S III]$  lines that we detect here can also be used to trace the ionization parameter and metallicity. There remains uncertainty over the reliability of NIRSpec flux calibrations as a function of wavelength, and so we prefer to only use ratios between emission lines that are close in wavelength. Additionally, we would require the application of extinction corrections to our data, given the large wavelength difference between  $[S III]$  and the other lines. As we do not have measurements of the  $H\beta$  flux, and therefore the Balmer decrement, our extinction corrections would be highly uncertain. Therefore we have elected not to use the  $[S III]$  lines in our analysis.

As a side note, a companion source to SPT0418-47 (SPT0418-47B) has been detected by Peng et al. (2022) and Cathey et al. (2023). While we are not focused on the nature of this source here, we note that we measure a metallicity of  $\sim 0.6\text{--}0.7 Z_{\odot}$  (applying the M13 calibration), which we find to be consistent with Peng et al. (2022). Therefore the smaller



**Figure 2.** Zoom-in 1D spectra of SPT0418-47 (top) and SPT2147-50 (bottom). All flux densities are in units of  $\text{erg cm}^{-2} \text{s}^{-1} \mu\text{m}^{-1}$ . The left panels show the integrated spectra, and the right panels show a sample typical  $3 \times 3$  binned spaxel, as used in the spatially resolved fitting. The emission lines are well modeled by Gaussians. We note that the integrated spectra are fit here with [S II] as shown in the plot, but for the binned spaxels we only fit H $\alpha$  and the [N II] doublet, as [S II] is typically too faint to be significantly detected in individual binned spaxels.

merging companion to SPT0418-47 is a slightly less metal-rich system.

A potential source of uncertainty in our metallicity estimates may arise from diffuse ionized gas (DIG), as the resolution of our observations is much greater than the scale of individual H II regions. Vale Asari et al. (2019) investigated this effect for star-forming galaxies in the MaNGA survey and found the diffuse component to have a  $\sim 0.1$  dex contribution to metallicity estimates derived using the [N II]/H $\alpha$  index, at the high-metallicity end. They also found the DIG to have a more prominent effect on the MZR at the high-stellar-mass end, where our sources (particularly SPT2147-50) lie. Similar findings were also made by Poetrodjojo et al. (2019). A correction for this potential effect is beyond the scope of this work, however.

In general, due to the systematic uncertainties in the different calibrations and the fact that these are derived for galaxies at much lower redshifts than the two SPT DSFGs, it is highly challenging to constrain their global metallicities confidently. However, even while being conservative over the possibility of AGN emission in the two DSFGs, we can confidently say that both are enriched to near-solar levels, likely as a result of their very high SFRs.

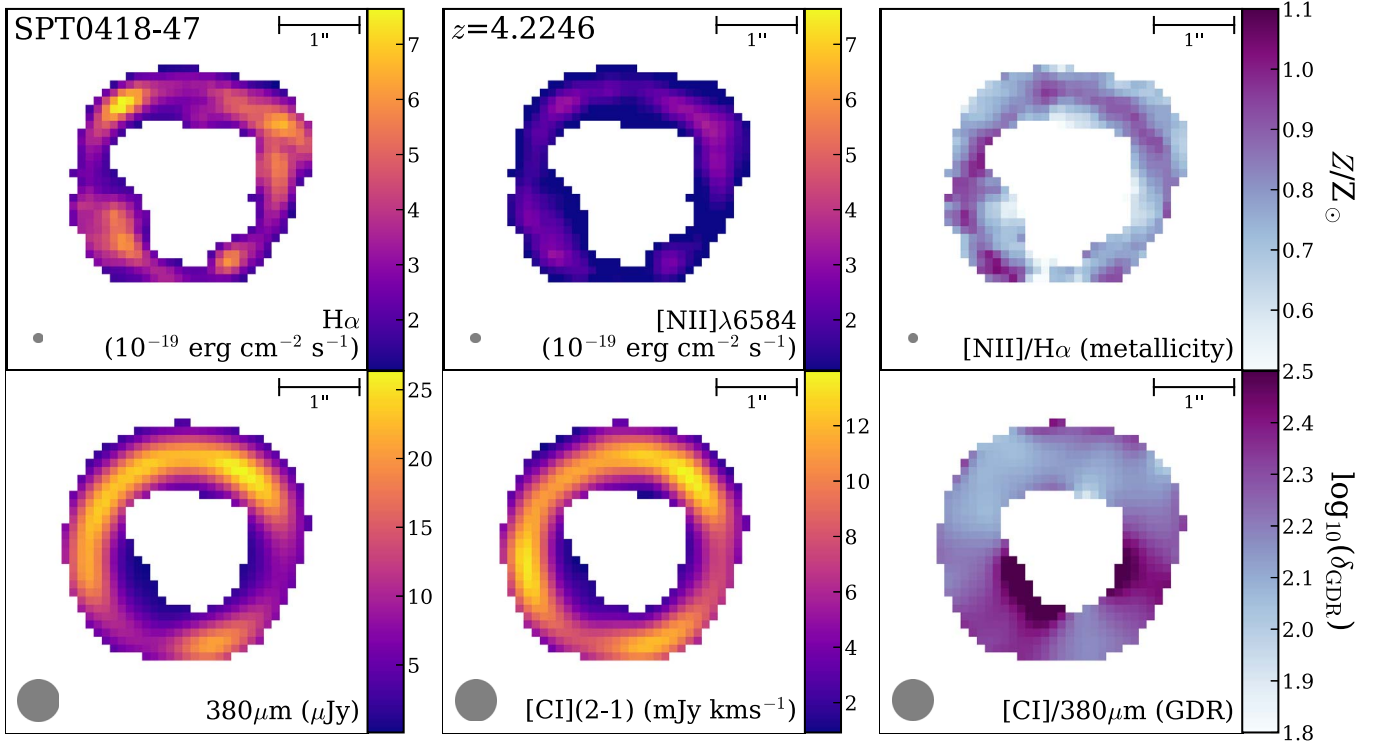
### 3.2. MZR and FMR

In general, galaxies appear to display a correlation between gas-phase metallicity and stellar mass, the so-called mass-metallicity relation (MZR; e.g., Tremonti et al. 2004). In addition, a “three-dimensional” relation between stellar mass, metallicity, and SFR

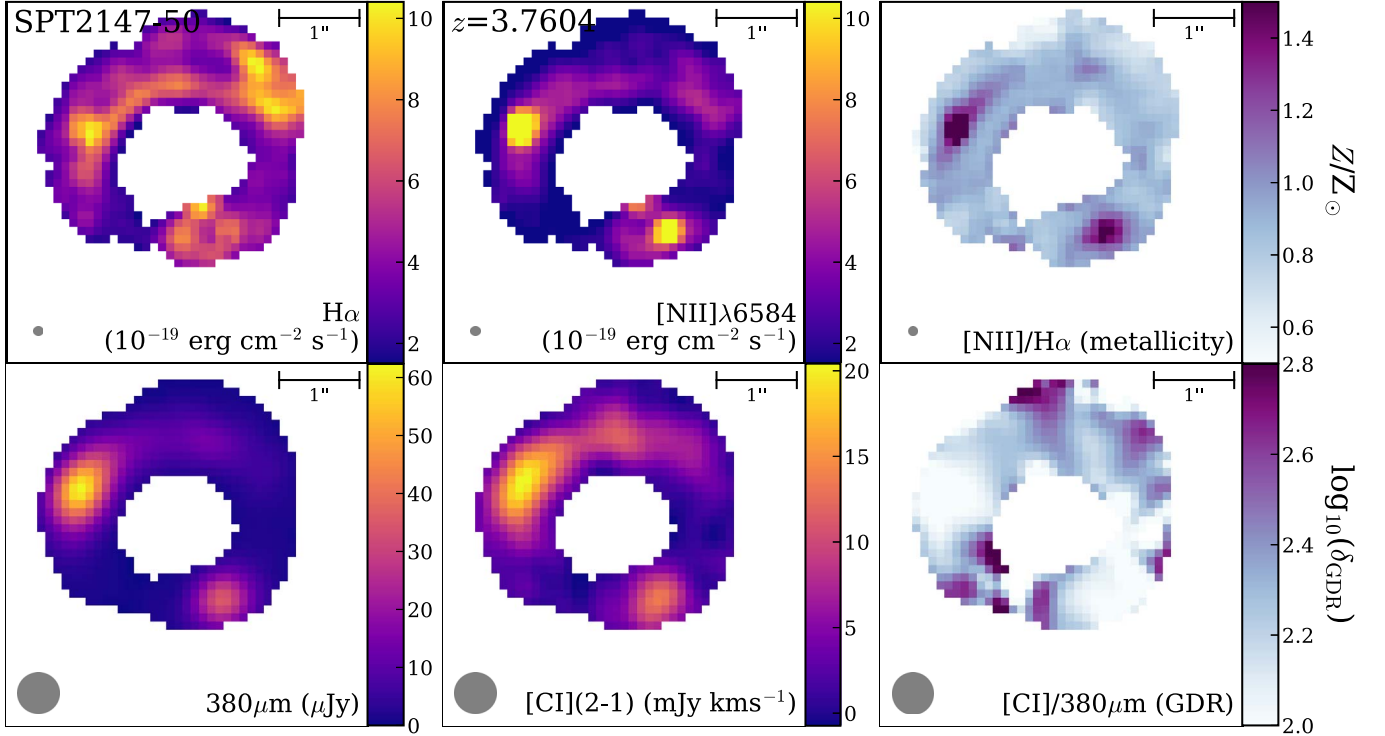
has been suggested and named the Fundamental Metallicity Relation (FMR; Mannucci et al. 2010). In the FMR, low-mass galaxies with higher SFRs typically contain a lower proportion of metals, and in high-mass galaxies the metallicity saturates and becomes independent of SFR (as in the MZR). Mannucci et al. (2010) found this relation to hold constant with low scatter up to  $z \sim 2.5$  (also see, e.g., Lara-López et al. 2010; Troncoso et al. 2014; C20), attributing the result to the dominance and consistency of smooth secular processes at low to intermediate redshifts, with this equilibrium being reached at least as early as  $z \sim 2.5$ .

At higher redshifts the picture is less clear. Mannucci et al. (2010) showed that galaxies at  $z \sim 2.5$  are offset from the FMR, specifically around 0.6 dex toward lower metallicities, which may imply that smooth secular processes are less prominent in higher-redshift sources. To test this for the two  $z \sim 4$  DSFGs, in Figure 5 we show the derived oxygen abundances  $12 + \log(\text{O}/\text{H})$  using the C20 calibration versus stellar masses derived from SED fitting with CIGALE (Cathey et al. 2023; K. A. Phadke et al. 2023, in preparation). The open points indicate the oxygen abundances derived from masking emission in pixels with [N II]/H $\alpha > 0.5$ , and are shifted horizontally for visual clarity.

For comparison with other similarly selected sources, we also include in Figure 5  $z \sim 2$  DSFGs with [N II]/H $\alpha$  measurements from the *K*-band Multi-Object Spectrograph (KMOS; Birkin 2022), along with  $z \sim 1.3$ – $2.6$  galaxies from the KMOS<sup>3D</sup> survey (Wisnioski et al. 2015), the latter of which is generally comprised of galaxies with lower SFRs than those studied in this work. The two DSFGs presented in this work are consistent with the



**Figure 3.** Top row: resolved H $\alpha$ , [N II], and [N II]/H $\alpha$  maps of SPT0418-47 from JWST/NIRSpec (left to right). The [N II]/H $\alpha$  map is used as a proxy for metallicity. Bottom row: ALMA rest-frame 380  $\mu$ m continuum and [C I] line maps, along with the resultant [C I]/380  $\mu$ m map (left to right). The [C I]/380  $\mu$ m map is used as a proxy for the gas-to-dust ratio. The gray circles show the approximate PSF of the data in each panel, and the horizontal bars in the top right of each panel indicate the scale of 1'' ( $\sim$ 0.7 kpc at  $z = 4$ ).

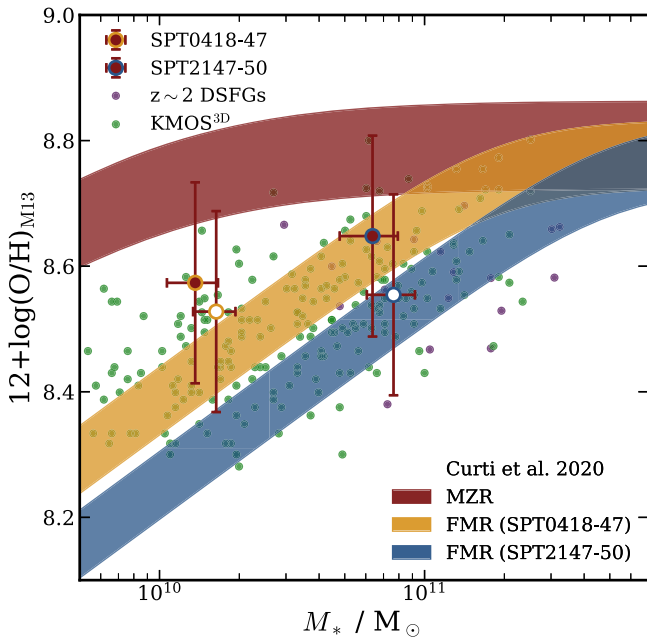


**Figure 4.** Same maps as presented in Figure 3, but this time for SPT2147-50. This source displays two regions of very intense [N II] emission which clearly match with regions of strong rest-frame 380  $\mu$ m and [C I] emission. Given that [N II]/H $\alpha$  > 1 in these regions, we are likely detecting emission from an active galactic nucleus (AGN).

majority of the comparison sources, albeit generally on the more metal-rich end.

From C20 we show the MZR for local galaxies, along with the FMR for the SFRs of the two galaxies (see Table 1),

including the scatter in both cases. Both galaxies are consistent with the local MZR within the uncertainties—they are high-mass galaxies, at which point the metallicity is expected to saturate at around  $12 + \log(\text{O}/\text{H}) \sim 8.7\text{--}8.8$ . According to the



**Figure 5.** Oxygen abundance  $12 + \log(\text{O}/\text{H})$  estimated from the  $[\text{N II}]/\text{H}\alpha$  ratio, using the **M13** calibration (see Section 3.1), vs. stellar mass estimated from SED fitting. As comparison samples we include galaxies from the **KMOS<sup>3D</sup>** survey (Wisnioski et al. 2015), and  $z \sim 1.5\text{--}2.5$  DSFGs also observed with **KMOS** (Birkin 2022). From **C20** we display the MZR (red shaded) and the FMR for the SFRs of the two galaxies (yellow for SPT0418-47, blue for SPT2147-50). The open points show how far down the points would move if we were to exclude pixels with  $[\text{N II}]/\text{H}\alpha > 0.5$  conservatively to account for AGN (the points are also shifted horizontally for visual clarity). Both DSFGs are consistent with the MZR, and are also consistent with the upper end of the FMR, particularly when we account for potential AGN emission.

FMR they are both marginally more metal rich than expected, although generally consistent within the large uncertainties, especially when we account for potential AGN emission.

Mannucci et al. (2010) claim that the relatively small scatter in the FMR up to  $z \sim 2.5$  implies constant relative significance of star formation and infall and outflows of gas. The two galaxies presented in this paper appear to have metallicities consistent with the FMR and could therefore fit into this picture. However, SPT0418-47 seems to be interacting with a companion (Peng et al. 2022; Cathey et al. 2023), which may be expected to drive it away from the FMR. Studies using both observations and simulations have shown that in the early stages of a merger the gas is diluted, thus lowering the metallicity. Subsequently, the metallicity is increased as the merger proceeds, when the SFR is enhanced (e.g., Rupke et al. 2008; Montuori et al. 2010; Rupke et al. 2010). It is therefore interesting that SPT0418-47 remains consistent with the FMR. We choose not to overinterpret this result given the large uncertainties on the oxygen abundances.

We note that we use the relations from **C20** as **M13** do not derive either the FMR or the MZR from their calibration. However, we note that we would expect both to move down if these relations were available for the **M13** calibration, and if anything this would place the two DSFGs  $\sim 0.2$  dex further above the FMR than we see in Figure 5. This would put both sources firmly above the FMR.

An important consideration to make is whether or not the line calibrations we assume are applicable at  $z \sim 4$ . There are few  $T_e$ -method-based metallicity measurements calibrated to

$\text{H}\alpha$  and  $[\text{N II}]$  at this epoch (although some work has been done with  $\text{H}\beta$  and  $[\text{O III}]$ ; e.g., Curti et al. 2023; Trump et al. 2023), hence our reliance on local calibrations, and it is possible DSFGs exhibit different relative abundances than nearby galaxies. For instance, a top-heavy initial mass function, as has been suggested as necessary to reconcile DSFG number counts with theory (e.g., Baugh et al. 2005), and therefore a large number of high-mass stars, would lead to a change in the relative abundances of nitrogen, oxygen, and hydrogen. A lack of observational data limits our ability to draw the correct conclusion, however some work on this topic has already been done with **NIRSpec**. For example, for  $z = 2.18$  galaxies Sanders et al. (2023) have found evidence that the local **C20**  $\text{N2}$  calibration for metallicity is biased  $\sim 0.5$  dex high when compared to direct measurements from auroral lines. This bias may be as significant, or potentially even worse, at  $z \sim 4$ .

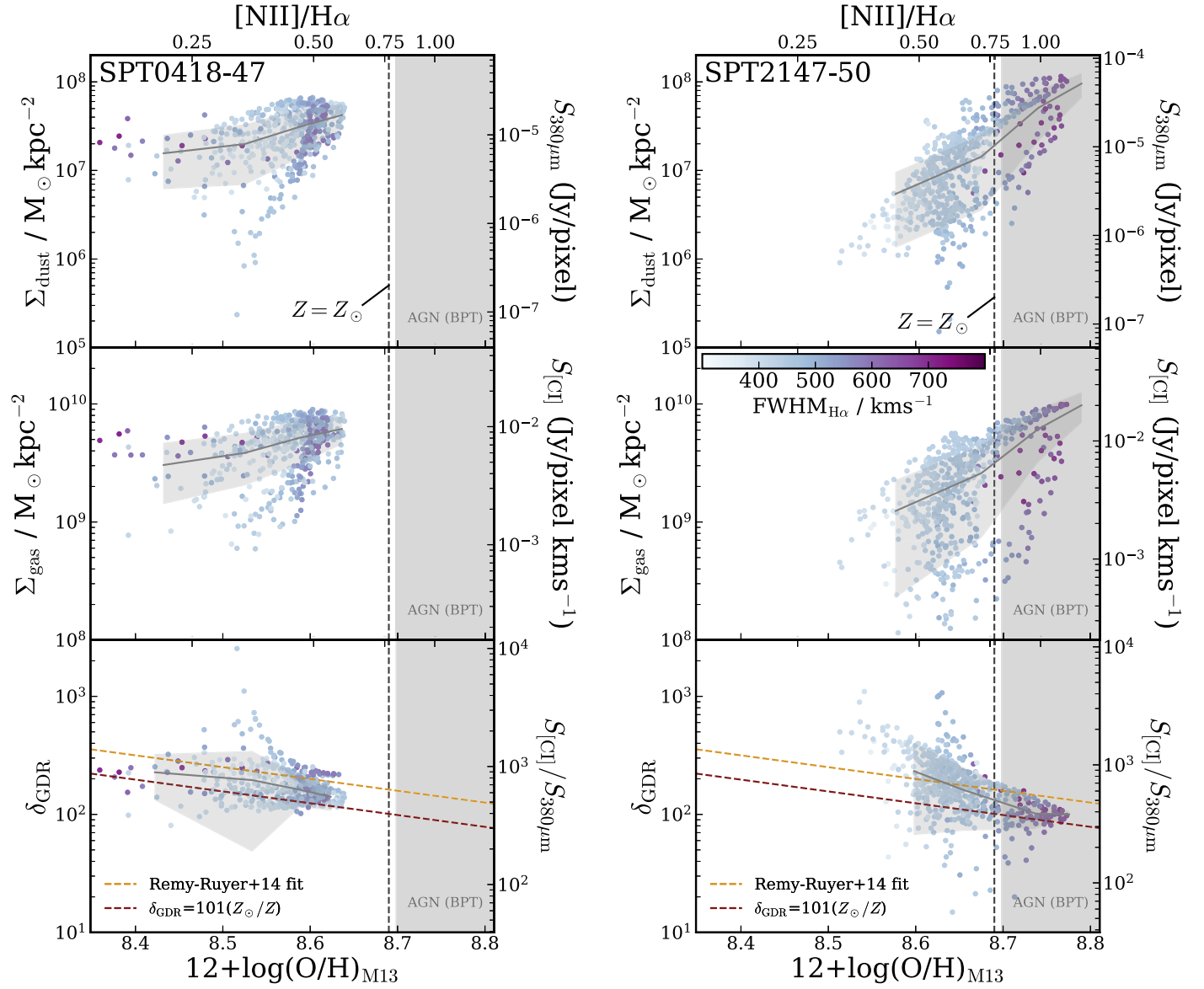
A further consideration is that if SPT2147-50 does in fact host an AGN that is contributing significantly to the IR emission, then this could result in a larger estimate of the SFR from SED fitting than the true value. This would in turn mean that the expected metallicity from the FMR is actually lower than it should be. Additionally, the SFRs used in the **C20** scaling relations are derived from  $\text{H}\alpha$  luminosities, scaled to a total SFR. Given the high levels of dust extinction in the two galaxies (see Table 1), we do not derive  $\text{H}\alpha$ -based SFRs in this work, as the corrections are likely to be significant and uncertain. We instead use total SFRs derived from **CIGALE** SED fitting, which uses the parameterization from Boquien et al. (2019), with the star formation histories modeled as an exponential decay ( $\tau_{\text{burst}} = 1$  Gyr) including an additional burst component using the stellar population model from Bruzual & Charlot (2003).

### 3.3. Resolved Metallicities and the Gas-to-dust Ratio

The impressive sensitivity and resolution of **JWST** has allowed us to resolve the  $[\text{N II}]/\text{H}\alpha$  flux ratio spatially (see Figures 3 and 4). We wish to compare these with the distribution of dust and gas in the two galaxies in order to determine how they are related. We therefore compare the  $[\text{N II}]/\text{H}\alpha$  maps from **NIRSpec** with existing **ALMA** imaging of the rest-frame  $380 \mu\text{m}$  continuum and  $[\text{C I}]$  line emission, which provide estimates of the dust and ISM masses.

Figures 3 and 4 show **ALMA** rest-frame  $380 \mu\text{m}$  continuum maps and  $[\text{C I}]$  emission line maps of the two DSFGs, the latter of which are derived by summing the flux within twice the FWHM of the line. We also show maps of the  $[\text{C I}]$  to  $380 \mu\text{m}$  ratio, which we use as a proxy for the gas-to-dust ratio ( $\delta_{\text{GDR}}$ ). Visually, these three maps are broadly consistent in terms of regions of high  $[\text{N II}]/\text{H}\alpha$  coinciding with regions of high flux in the **ALMA** maps. This is most clear in SPT2147-50, which displays two bright regions in the  $380 \mu\text{m}$  maps that are also present in the **NIRSpec** data.

To quantify the relation between the metallicity, gas, and dust, we convert the **ALMA** maps to dust and gas mass surface density  $\Sigma_{\text{dust}}$  and  $\Sigma_{\text{gas}}$  and plot both versus  $[\text{N II}]/\text{H}\alpha$  on a pixel-by-pixel basis, as shown in Figure 6. To convert the **ALMA** rest-frame  $380 \mu\text{m}$  continuum maps to dust mass maps we apply Equation (1) of Dunne et al. (2003), assuming a dust mass opacity coefficient at  $125 \mu\text{m}$  of  $2.64 \text{ m}^2 \text{ kg}^{-1}$ , a dust temperature  $T_{\text{dust}}$  of 40 K, and extrapolating to  $380 \mu\text{m}$  with dust emissivity index  $\beta = 2.0$ .



**Figure 6.** Spaxel-by-spaxel ( $0''.1, \sim 0.7$  kpc) variation of  $380\ \mu\text{m}$  flux (top), [C I] line flux (middle), and [C I]/ $380\ \mu\text{m}$  flux ratio (bottom) as a function of [N II]/ $H\alpha$  line ratio for the two SPT DSGs. On the top axes we show the corresponding oxygen abundances according to the calibration of M13. On the right axes we show the corresponding dust mass surface density  $\Sigma_{\text{dust}}$ , gas mass surface density  $\Sigma_{\text{gas}}$ , and gas-to-dust ratio  $\delta_{\text{GDR}}$ , using the conversions described in Section 3.3. We plot a binned median (gray line) with  $1\sigma$  scatter (gray region), and color code points by  $H\alpha$  FWHM. We also indicate solar metallicity (Asplund et al. 2021) and shade the region where [N II]/ $H\alpha > 0.8$ , the latter of which is likely to be contaminated to some extent by AGN emission. Notably, in this region  $H\alpha$  emission is broadest when compared to the rest of the source. In both sources the gas-to-dust ratio appears to decline with increasing metallicity, although this trend is more prominent in SPT2147-50. In the bottom panels we also show models from Rémy-Ruyer et al. (2014) and Aniano et al. (2020), which are discussed further in Section 3.3.

This approach ignores any potential variations in  $T_{\text{dust}}$  and  $\beta$ . However, Spilker et al. (2023) recently analyzed rest-frame 120 and  $160\ \mu\text{m}$  data from SPT0418-47 and found no evidence of significant variations in dust temperature across the source. If indeed we are seeing AGN emission in SPT2147-50 then we may expect these regions to display higher dust temperatures, but we flag regions of the parameter space in Figure 6 where this is likely to be the case and avoid overinterpreting these regions. There has yet to be significant study of variations in the dust emissivity across individual galaxies, and indeed we cannot rule this out in our sources.

To convert the [C I] emission line maps to molecular gas mass maps we use Equation (6) of Bothwell et al. (2017), except in our case we use the Einstein  $A_{21} = 2.68 \times 10^{-7}\ \text{s}^{-1}$  coefficient (Papadopoulos & Greve 2004) and excitation factor

$Q_{21} = 0.22$  (Dunne et al. 2022) for the [C I](2–1) transition instead of the [C I](1–0) values. Following Papadopoulos & Greve (2004) and Bothwell et al. (2017) we adopt a [C I]/ $H_2$  abundance ratio of  $X_{[\text{C I}]} = 3 \times 10^{-5}$ . This is a commonly adopted value in the literature, but we note that this value cannot be measured for high- $z$  galaxies and is therefore based on measurements from local galaxies. It is therefore subject to considerable uncertainty. Indeed, through a comparison with dust-based gas masses, Bothwell et al. (2017) suggested that a higher value of  $X_{[\text{C I}]} = 7 \times 10^{-5}$  could also be reasonable. Given that we are primarily concerned with the variation of  $\delta_{\text{GDR}}$  with metallicity, rather than its absolute value, this assumption should not significantly affect our conclusions.

In Figure 6 we plot three quantities as a function of [N II]/ $H\alpha$ , a proxy for metallicity. These are  $S_{380\ \mu\text{m}}$ ,  $S_{[\text{C I}]}$  and  $S_{[\text{C I}]} / S_{380\ \mu\text{m}}$ ,



which we use as proxies for dust mass surface density, gas mass surface density, and gas-to-dust ratio, respectively. The points are color coded by  $H\alpha$  FWHM. Given the various caveats and assumptions which come with these proxies, we choose to plot both the observed and converted quantities. Our interpretation will mostly focus on the variation of these properties rather than their absolute values. Additionally, all corresponding panels are shown on the same scale (of absolute values) to enable a direct comparison between the two galaxies. We also indicate solar metallicity and shade the region where  $[N II]/H\alpha > 0.8$ , which the BPT diagram suggests is likely to result from AGN emission.

First, we note that in both galaxies, there appears to be a positive correlation between dust/gas mass surface density and metallicity. This indicates that regions containing more gas and dust are also more metal rich. This trend is stronger in SPT2147-50, in which we see that the most metal-rich regions also display the broadest  $H\alpha$  emission. Given that these points fall within the shaded region, it is likely that the most “metal-rich” regions of SPT2147-50 are in fact regions of AGN emission. This is a striking conclusion given that no clear AGN have previously been identified in any SPT-selected DSFG, including some objects more extreme than those targeted here (e.g., Ma et al. 2016; Apostolovski et al. 2019). It is theorized that DSFGs proceed to evolve through a quasi-stellar object phase (Blain et al. 2002; Swinbank et al. 2006; Hopkins et al. 2008), and therefore we may be observing the beginnings of this evolution in SPT2147-50. NIRSPEC follow up should be proposed for other sources in the SPT DSFG sample, in order to identify any further AGN candidates.

Turning to the bottom panels, we see that the gas-to-dust ratio appears to decline with increasing metallicity, a result that has been observed in local galaxies (e.g., Leroy et al. 2011; Rémy-Ruyer et al. 2014; Aniano et al. 2020). In the bottom panels of Figure 6 we plot two models to compare with our data. We show the model fit by Rémy-Ruyer et al. (2014) to 126 local galaxies spanning  $\sim 2$  dex in metallicity, derived from strong-line calibrations. Next we include a simple model from Aniano et al. (2020) in which the gas-to-dust ratio is estimated assuming that essentially all heavy elements are in dust grains, with solar relative abundances. This results in a linear relation between metallicity and  $\delta_{GDR}$ . Both models appear to match the results from both galaxies within the uncertainties. Even if we ignore the absolute values, the trend of decreasing  $\delta_{GDR}$  with metallicity is generally well described by both models. We tentatively conclude that the gas-to-dust ratio and its variation with metallicity in these two DSFGs is consistent with findings from local galaxies, which is not necessarily unexpected but has not yet been shown for DSFGs as distant as the two we present in this paper.

#### 4. Conclusions

We have presented two of the first spatially resolved metallicity maps of DSFGs at  $z \sim 4$ , utilizing IFU observations with JWST/NIRSPEC. Both sources are detected in  $H\alpha$  and  $[N II]$  at very high S/N, enabling us to perform resolved spectroscopy of these lensed systems. We find both SPT0418-47 and SPT2147-50 to be enriched to near-solar metallicity (conservatively  $\sim 0.7 Z_{\odot}$ ), with evidence for AGN-like  $[N II]/H\alpha$  ratios and broad  $H\alpha$  emission. The derived oxygen abundances are consistent with the FMR for both galaxies. Through a direct comparison with ALMA rest-frame  $380 \mu\text{m}$  continuum and  $[C I]$  line maps at matched resolution, which we

use as proxies for dust and gas mass, respectively, we find that the gas-to-dust ratio is negatively correlated with the metallicity, a result that is consistent with literature studies of local galaxies. At least qualitatively, it appears that these early-Universe dusty galaxies bear some resemblance to expectations from  $z \sim 0$  galaxies, even on highly resolved spatial scales.

In the absence of  $[O III]$  and  $H\beta$  coverage we interpret these results with caution, as the possibility remains that regions of high  $[N II]/H\alpha$  are actually the result of AGN emission. Furthermore, detailed lens modeling analysis and source plane reconstruction of these data have not yet been carried out; this will be explored in future work. Regardless, this work presents the first resolved metallicity maps in DSFGs at  $z \sim 4$ , and the data quality shows the potential of JWST to further our understanding of the processes that shape the ISM in high-redshift DSFGs.

#### Acknowledgments

T.A.H. is supported by an appointment to the NASA Postdoctoral Program (NPP) at NASA Goddard Space Flight Center, administered by Oak Ridge Associated Universities under contract with NASA. The SPT is supported by the NSF through grant OPP-1852617. J.D.V. and K.P. acknowledge support from the US NSF under grants AST-1715213 and AST-1716127. J.D.V. acknowledges support from an A. P. Sloan Foundation Fellowship. J.S.S. is supported by NASA Hubble Fellowship grant No. HF2-51446 awarded by the Space Telescope Science Institute, which is operated by the Association of Universities for Research in Astronomy, Inc., for NASA, under contract NAS 5-26555. D.N. acknowledges support from the US NSF under grant 1715206 and Space Telescope Science Institute under grant AR-15043.0001 M.A. acknowledges support from FONDECYT grant 1211951, ANID+PCI+INSTITUTO MAX PLANCK DE ASTRONOMIA MPG 190030, ANID+PCI+REDES 190194, and ANID BASAL project FB210003. JWST is operated by the Space Telescope Science Institute under the management of the Association of Universities for Research in Astronomy, Inc., under NASA contract No. NAS 5-03127. The National Radio Astronomy Observatory is a facility of the National Science Foundation operated under cooperative agreement by Associated Universities, Inc. This paper makes use of the following ALMA data: ADS/JAO.ALMA#2018.1.01060.S and ADS/JAO.ALMA#2021.1.00252.S. ALMA is a partnership of ESO (representing its member states), NSF (USA) and NINS (Japan), together with NRC (Canada), MOST and ASIAA (Taiwan), and KASI (Republic of Korea), in cooperation with the Republic of Chile. The Joint ALMA Observatory is operated by ESO, AUI/NRAO, and NAOJ.

*Facilities:* JWST and ALMA.

*Software:* astropy (Astropy Collaboration et al. 2018) and CASA (McMullin et al. 2007).

#### ORCID iDs

Jack E. Birkin  <https://orcid.org/0000-0002-3272-7568>

Taylor A. Hutchison  <https://orcid.org/0000-0001-6251-4988>

Brian Welch  <https://orcid.org/0000-0003-1815-0114>

Justin S. Spilker  <https://orcid.org/0000-0003-3256-5615>

Manuel Aravena  <https://orcid.org/0000-0002-6290-3198>

Matthew B. Bayliss  <https://orcid.org/0000-0003-1074-4807>

Jared Cathey  <https://orcid.org/0000-0002-4657-7679>

Anthony H. Gonzalez  <https://orcid.org/0000-0002-0933-8601>  
 Gayathri Gururajan  <https://orcid.org/0000-0002-7472-7697>  
 Christopher C. Hayward  <https://orcid.org/0000-0003-4073-3236>  
 Gourav Khullar  <https://orcid.org/0000-0002-3475-7648>  
 Keunho J. Kim  <https://orcid.org/0000-0001-6505-0293>  
 Guillaume Mahler  <https://orcid.org/0000-0003-3266-2001>  
 Matthew A. Malkan  <https://orcid.org/0000-0001-6919-1237>  
 Desika Narayanan  <https://orcid.org/0000-0002-7064-4309>  
 Grace M. Olivier  <https://orcid.org/0000-0002-4606-4240>  
 Kedar A. Phadke  <https://orcid.org/0000-0001-7946-557X>  
 Cassie Reuter  <https://orcid.org/0000-0001-7477-1586>  
 Jane R. Rigby  <https://orcid.org/0000-0002-7627-6551>  
 J. D. T. Smith  <https://orcid.org/0000-0003-1545-5078>  
 Manuel Solimano  <https://orcid.org/0000-0001-6629-0379>  
 Nikolaus Sulzenauer  <https://orcid.org/0000-0002-3187-1648>  
 Joaquin D. Vieira  <https://orcid.org/0000-0001-7192-3871>  
 David Vizgan  <https://orcid.org/0000-0001-7610-5544>  
 Axel Weiss  <https://orcid.org/0000-0003-4678-3939>

## References

- Aniano, G., Draine, B. T., Hunt, L. K., et al. 2020, *ApJ*, 889, 150  
 Apostolovski, Y., Aravena, M., Anguita, T., et al. 2019, *A&A*, 628, A23  
 Aravena, M., Spilker, J. S., Bethermin, M., et al. 2016, *MNRAS*, 457, 4406  
 Asplund, M., Amarsi, A. M., & Grevesse, N. 2021, *A&A*, 653, A141  
 Astropy Collaboration, Price-Whelan, A. M., & Sipőcz, B. M. 2018, *AJ*, 156, 123  
 Baldwin, J. A., Phillips, M. M., & Terlevich, R. 1981, *PASP*, 93, 5  
 Bassini, L., Feldmann, R., Gensior, J., et al. 2023, *MNRAS*, 525, 5388  
 Baugh, C. M., Lacey, C. G., Frenk, C. S., et al. 2005, *MNRAS*, 356, 1191  
 Birkin, J. E. 2022, PhD thesis, Univ. Durham  
 Birkin, J. E., Weiss, A., Wardlow, J. L., et al. 2021, *MNRAS*, 501, 3926  
 Blain, A. W., Smail, I., Ivison, R. J., Kneib, J. P., & Frayer, D. T. 2002, *PhR*, 369, 111  
 Böker, T., Beck, T. L., Birkmann, S. M., et al. 2023, *PASP*, 135, 038001  
 Boquien, M., Burgarella, D., Roehlly, Y., et al. 2019, *A&A*, 622, A103  
 Bothwell, M. S., Aguirre, J. E., Aravena, M., et al. 2017, *MNRAS*, 466, 2825  
 Bruzual, G., & Charlot, S. 2003, *MNRAS*, 344, 1000  
 Bushouse, H., Eisenhamer, J., Dencheva, N., et al., 2023 JWST Calibration Pipeline, v1.10.2 Zenodo, doi:10.5281/zenodo.7829329  
 Bussmann, R. S., Riechers, D., Fialkov, A., et al. 2015, *ApJ*, 812, 43  
 Casey, C. M., Narayanan, D., & Cooray, A. 2014, *PhR*, 541, 45  
 Cathey, J., Gonzalez, A. H., Lower, S., et al. 2023, arXiv:2307.10115  
 Curti, M., D'Eugenio, F., Carniani, S., et al. 2023, *MNRAS*, 518, 425  
 Curti, M., Mannucci, F., Cresci, G., & Maiolino, R. 2020, *MNRAS*, 491, 944  
 Davé, R., Finlator, K., Oppenheimer, B. D., et al. 2010, *MNRAS*, 404, 1355  
 De Breuck, C. 2019, *A&A*, 631, A167  
 Dopita, M. A., Kewley, L. J., Sutherland, R. S., & Nicholls, D. C. 2016, *Ap&SS*, 361, 61  
 Dudzevičiūtė, U., Smail, I., Swinbank, A. M., et al. 2020, *MNRAS*, 494, 3828  
 Dunne, L., Eales, S. A., & Edmunds, M. G. 2003, *MNRAS*, 341, 589  
 Dunne, L., Maddox, S. J., Papadopoulos, P. P., Ivison, R. J., & Gomez, H. L. 2022, *MNRAS*, 517, 962  
 Endsley, R., Stark, D. P., Lyu, J., et al. 2023, *MNRAS*, 520, 4609  
 Everett, W. B., Zhang, L., Crawford, T. M., et al. 2020, *ApJ*, 900, 55  
 Gardner, J. P., Mather, J. C., Abbott, R., et al. 2023, *PASP*, 135, 068001  
 Gillman, S., Puglisi, A., Dudzevičiūtė, U., et al. 2022, *MNRAS*, 512, 3480  
 Harrington, K. C., Yun, M. S., Cybulski, R., et al. 2016, *MNRAS*, 458, 4383  
 Hayward, C. C., Sparre, M., Chapman, S. C., et al. 2021, *MNRAS*, 502, 2922  
 Hopkins, P. F., Hernquist, L., Cox, T. J., & Kereš, D. 2008, *ApJS*, 175, 356  
 Kamienieski, P. S., Yun, M. S., Harrington, K. C., et al. 2023, arXiv:2301.09746  
 Kewley, L. J., Dopita, M. A., Leitherer, C., et al. 2013, *ApJ*, 774, 100  
 Kewley, L. J., Groves, B., Kauffmann, G., & Heckman, T. 2006, *MNRAS*, 372, 961  
 Lacey, C. G., Baugh, C. M., Frenk, C. S., et al. 2016, *MNRAS*, 462, 3854  
 Lara-López, M. A., Cepa, J., Bongiovanni, A., et al. 2010, *A&A*, 521, L53  
 Leroy, A. K., Bolatto, A., Gordon, K., et al. 2011, *ApJ*, 737, 12  
 Ma, J., Gonzalez, A. H., Spilker, J. S., et al. 2015, *ApJ*, 812, 88  
 Ma, J., Gonzalez, A. H., Vieira, J. D., et al. 2016, *ApJ*, 832, 114  
 Maiolino, R., & Mannucci, F. 2019, *A&ARv*, 27, 3  
 Mannucci, F., Cresci, G., Maiolino, R., Marconi, A., & Gnerucci, A. 2010, *MNRAS*, 408, 2115  
 Marino, R. A., Rosales-Ortega, F. F., Sánchez, S. F., et al. 2013, *A&A*, 559, A114  
 Marrone, D. P., Spilker, J. S., Hayward, C. C., et al. 2018, *Natur*, 553, 51  
 Marsden, D., Gralla, M., Marriage, T. A., et al. 2014, *MNRAS*, 439, 1556  
 McAlpine, S., Smail, I., Bower, R. G., et al. 2019, *MNRAS*, 488, 2440  
 McElwain, M. W., Feinberg, L. D., Perrin, M. D., et al. 2023, *PASP*, 135, 058001  
 McMullin, J. P., Waters, B., Schiebel, D., Young, W., & Golap, K. 2007, in ASP Conf. Ser. 376, *Astronomical Data Analysis Software and Systems XVI*, ed. R. A. Shaw, F. Hill, & D. J. Bell (San Francisco, CA: ASP), 127  
 Menzel, M., Davis, M., Parrish, K., et al. 2023, *PASP*, 135, 058002  
 Montuori, M., Di Matteo, P., Lehnert, M. D., Combes, F., & Semelin, B. 2010, *A&A*, 518, A56  
 Negrello, M., Hopwood, R., De Zotti, G., et al. 2010, *Sci*, 330, 800  
 Osterbrock, D. E., & Ferland, G. J. 2006, *Astrophysics of Gaseous Nebulae and Active Galactic Nuclei* (Mill Valley, CA: Univ. Science Books)  
 Papadopoulos, P. P., & Greve, T. R. 2004, *ApJL*, 615, L29  
 Peng, B., Lamarche, C., Stacey, G. J., et al. 2021, *ApJ*, 908, 166  
 Peng, B., Vishwas, A., Stacey, G., et al. 2023, *ApJL*, 944, L36  
 Pérez-Montero, E., & Contini, T. 2009, *MNRAS*, 398, 949  
 Pettini, M., & Pagel, B. E. J. 2004, *MNRAS*, 348, L59  
 Pilyugin, L. S., & Grebel, E. K. 2016, *MNRAS*, 457, 3678  
 Planck Collaboration, Aghanim, N., & Akrami, Y. 2020, *A&A*, 641, A6  
 Poetrodjojo, H., D'Agostino, J. J., Groves, B., et al. 2019, *MNRAS*, 487, 79  
 Poetrodjojo, H., Groves, B., Kewley, L. J., et al. 2021, *MNRAS*, 502, 3357  
 Rémy-Ruyer, A., Madden, S. C., Galliano, F., et al. 2014, *A&A*, 563, A31  
 Reuter, C., Spilker, J. S., Vieira, J. D., et al. 2023, *ApJ*, 948, 44  
 Reuter, C., Vieira, J. D., Spilker, J. S., et al. 2020, *ApJ*, 902, 78  
 Rigby, J., Perrin, M., McElwain, M., et al. 2023a, *PASP*, 135, 048001  
 Rigby, J. R., Lightsey, P. A., García Marín, M., et al. 2023b, *PASP*, 135, 048002  
 Rupke, D. S. N., Kewley, L. J., & Chien, L. H. 2010, *ApJ*, 723, 1255  
 Rupke, D. S. N., Veilleux, S., & Baker, A. J. 2008, *ApJ*, 674, 172  
 Rybak, M., Hodge, J. A., Greve, T. R., et al. 2022, *A&A*, 667, A70  
 Sanders, R. L., Shapley, A. E., Clarke, L., et al. 2023, *ApJ*, 943, 75  
 Sanders, R. L., Shapley, A. E., Kriek, M., et al. 2015, *ApJ*, 799, 138  
 Sanders, R. L., Shapley, A. E., Reddy, N. A., et al. 2020, *MNRAS*, 491, 1427  
 Spilker, J. S., Aravena, M., Marrone, D. P., et al. 2015, *ApJ*, 811, 124  
 Spilker, J. S., Marrone, D. P., Aguirre, J. E., et al. 2014, *ApJ*, 785, 149  
 Spilker, J. S., Marrone, D. P., Aravena, M., et al. 2016, *ApJ*, 826, 112  
 Spilker, J. S., Phadke, K. A., Aravena, M., et al. 2023, *Natur*, 618, 708  
 Steidel, C. C., Rudie, G. C., Strom, A. L., et al. 2014, *ApJ*, 795, 165  
 Strandet, M. L., Weiss, A., De Breuck, C., et al. 2017, *ApJL*, 842, L15  
 Sun, F., Egami, E., Fujimoto, S., et al. 2022, *ApJ*, 932, 77  
 Swinbank, A. M., Chapman, S. C., Smail, I., et al. 2006, *MNRAS*, 371, 465  
 Swinbank, A. M., Simpson, J. M., Smail, I., et al. 2014, *MNRAS*, 438, 1267  
 Tremonti, C. A., Heckman, T. M., Kauffmann, G., et al. 2004, *ApJ*, 613, 898  
 Troncoso, P., Maiolino, R., Sommariva, V., et al. 2014, *A&A*, 563, A58  
 Trump, J. R., Arrabal Haro, P., Simons, R. C., et al. 2023, *ApJ*, 945, 35  
 Vale Asari, N., Couto, G. S., Cid Fernandes, R., et al. 2019, *MNRAS*, 489, 4721  
 Vieira, J. D., Marrone, D. P., Chapman, S. C., et al. 2013, *Natur*, 495, 344  
 Wisnioski, E., Förster Schreiber, N. M., Wuyts, S., et al. 2015, *ApJ*, 799, 209  
 Wuyts, E., Kurk, J., Förster Schreiber, N. M., et al. 2014, *ApJL*, 789, L40  
 Zavala, J. A., Casey, C. M., Manning, S. M., et al. 2021, *ApJ*, 909, 165